Int. J. Plasma Environ. Sci. Technol. 18 (2024) e02005 (10p)

International Journal of
Plasma Environmental Science and Technology

Regular Paper

DOI: 10.34343/ijpest.2024.18.e02005

CO_2 methanation through gliding arc discharge over Ni/Al_2O_3

Ming Li, Dae-Yeong Kim, Shutaro Nakao, Tomohiro Nozaki*

Department of Mechanical Engineering, Tokyo Institute of Technology, Tokyo 152-8550, Japan

* Corresponding author: nozaki.t.ab@m.titech.ac.jp (Tomohiro Nozaki)

Received: 28 May 2024
Revised: 7 August 2024
Accepted: 8 August 2024

Abstract

This research investigates the catalytic performance of Ni/Al_2O_3 in the methanation of CO_2 under both thermal and Gliding Arc Discharge (GAD) conditions. Utilizing *in situ* transmission infrared (TIR) absorption spectroscopy and quadrupole mass spectrometry (QMS), the study analyzes the transient behavior of the plasma-catalyst interaction of CO_2 methanation. GAD significantly enhances CO_2 conversion and methane production compared to thermal catalysis by CO_2 activation, facilitating the rapid transformation of intermediate species on the catalyst surface. Additionally, the study provides a detailed analysis of the electrical characteristics of GAD, capturing voltage and current waveforms that illustrate the transient arc behavior under different phases of the discharge process. The results indicate that lower pressures, while reducing overall CO_2 conversion, enhance methane production by suppressing the gas phase CO_2 conversion to CO and promoting surface reactions. This comprehensive study not only advances the understanding of plasma-assisted catalysis for CO_2 methanation but also highlights the potential of this technology for enhancing greenhouse gas utilization with renewable energy-driven plasma, paving the way for future optimization and industrial application.

Keywords: CO_2 methanation, Gliding arc discharge, Ni/Al_2O_3, *in situ* TIR.

---

1. Introduction

The urgent challenge of sustainable energy production, coupled with effective greenhouse gas management, has catalyzed the exploration of innovative technological solutions. Among these, the methanation of carbon dioxide (CO_2) through catalytic processes presents a promising strategy for both sequestering CO_2 and generating methane, a versatile and valuable fuel [1–3]. Recent advancements in plasma-assisted catalysis [4-9], specifically through the application of Gliding Arc Discharge (GAD), offer a novel approach to CO_2 conversion, potentially surpassing conventional methods in efficiency due to higher electron energy outputs that favor enhanced CO_2 activation [7]. In conventional thermal catalysis systems, CO_2 methanation involves the hydrogenation of CO_2 to produce methane and water, a reaction that is thermodynamically feasible yet kinetically limited at lower temperatures [10, 11]. Specifically, while the conversion of CO_2can approach 100% conversion at temperatures below 200 °C, these conditions are not typically conducive to methanation due to slower reaction kinetics [12]. Compared to conventional thermal catalysis, plasma technologies, particularly nonthermal plasma such as dielectric barrier discharge (DBD), are widely recognized for plasma and catalyst combined system [12–16]. These technologies enable the CO_2 methanation at lower temperatures, thereby reducing energy consumption and enhancing the conversion of CO_2. However, GAD, as a warm plasma, combines the advantages of both thermal and nonthermal plasma technologies [17]. It possesses a relatively high energy density, characterized by its ability to provide thermal energy equivalent to 1000 °C and various radicals simultaneously, which are crucial for the effective activation of CO_2 molecules [12]. Vibrational excitation of CO_2 molecules is important in the hydrogenation of CO_2. While the energy required for significant vibrational excitation cannot be adequately provided by temperature alone or by conventional low-temperature plasma [18,19]. Plasma, however, offers both aspects of energy, making it a highly valuable feature for the substantial conversion of CO_2, when it is combined with heterogeneous catalysts.

Despite the potential advantages of GAD, its application in CO_2 methanation has been limited by the high risk of catalyst deactivation due to direct interaction between the plasma and the catalyst [20, 21]. To address this, the current research employs a segmented reactor design that spatially separates the generation of GAD from the catalyst, thus preserving the catalytic activity and extending the life of the catalyst. Furthermore, nickel catalysts strike an effective balance between catalytic activity, cost, processability, and environmental compatibility, making them widely utilized in the methanation of CO_2 [22]. The extensive research conducted on nickel-based catalysts is also pivotal for understanding the role of GAD in methanation processes. These catalysts not only offer cost-effectiveness but also exhibit significant performance in terms of CO_2 conversion and methane yield at lower temperatures, a crucial aspect given the kinetic limitations of the methanation reaction.

In this study, we employed a Ni/Al_2O_3 and compared its catalytic performance under decompressed conditions (80 kPa ,40 kPa and 10 kPa) using both thermal and GAD catalysis. Additionally, we utilized *in situ* transmission infrared (TIR) absorption spectroscopy and quadrupole mass spectrometry (QMS) to understand the reaction mechanisms and monitor the dynamic behavior of methanation process. This paper aims to explore the potential of GAD-catalyzed CO_2 methanation, using innovative approaches to overcome conventional limitations.

2. Experimental

2.1 Catalyst preparation

An aqueous solution of urea was gradually added to a vigorously stirred mixture of γ-Al_2O_3 (99.9%, Kojundo Chemical Lab) and an aqueous solution of $Ni(NO_3)_2 \cdot 6H_2O$ (99%, FUJIFILM Wako) in a glass beaker. The addition was controlled to ensure uniform mixing. The mixture was tightly sealed with plastic film to prevent evaporation and heated while stirring continuously on a hot plate. The temperature was maintained at 90 °C for 5 hours to allow complete deposition of nickel onto the alumina support. After the deposition, the colorless supernatant was carefully decanted, and the resulting solid was collected. The solid was washed three times with deionized water to remove any residual urea and nitrates. The washed solid was then dried under reduced pressure at room temperature to remove excess moisture. The resulting powder was calcined at 500 °C for 1 hour to decompose the nickel nitrate into nickel oxide and to enhance the adhesion of nickel to the alumina. Finally, the calcined powder was reduced in a tubular furnace at 600 °C under a 50 mL min^{-1} flow of hydrogen gas for 1 hour to convert the nickel oxide to metallic nickel, forming the active catalyst.

2.2 Experimental system and conditions

As illustrated in Fig. 1, the hydrogenation of CO_2 was conducted in an *in situ* TIR reactor equipped with a set of metallic electrodes to generate GAD inside of the cell. This reactor comprises a cylindrical quartz tube and an electric furnace, with a K-type thermocouple (outer diameter of 1 mm) installed to continuously monitor the temperature within the reactor. Stainless steel high-voltage electrode and ground electrode, each 1 mm in diameter, were inserted into the reactor, with an electrode gap of 10 mm. The electrical parameters of GAD were monitored using an oscilloscope (RIGOL MSO-5) connected to the reactor via a high-voltage probe, with the voltage waveform peak-to-peak value set at 9 kV throughout the entire experiment, powered by an inverter-controlled neon transformer (Lecip Co. ALPHA NEON M-5). Discharge current was measured by the potential drop between 1 kΩ electrical resistance connected in series on the ground side.

Catalyst powder, ranging from 25–30 mg, was evenly distributed into a disk kit and compressed using a press to form small pellets (diameter of 10 mm and thickness of 1 mm). Subsequently, the catalyst was secured on a glass support and positioned 5 mm downstream of the discharge zone. *In situ* TIR spectra were collected using a Fourier Transform Infrared Spectrometer (FTIR, JASCO FTIR-6600 Type A) equipped with a Mercury-Cadmium-Telluride (MCT) detector, scanning 44 times within the range of 4000-600 cm^{-1} at a spectral resolution of 4 cm^{-1}. Spectra were recorded every 30 seconds. Before the reaction, the catalyst was reduced in a flow of 9%H2/Ar (110 mL min^{-1}) at a heating rate of 30 °C min^{-1} to 600 °C and held at this temperature for 1 hour. Upon cooling the reactor to 250 °C, a typical feed gas mixture comprising 10 mL min^{-1} CO_2, 40 mL min^{-1} H_2, and 110 mL min^{-1} Ar was introduced for CO_2 hydrogenation. Additionally, to further understand the evolution of surface-adsorbed species on the catalyst under thermal and GAD conditions transient experiments were conducted by alternating H_2/Ar and CO_2/Ar flows. Ar served as a balance gas to dilute the reactant gases, preventing infrared spectrum signal saturation. A programmable mass flow controller controlled gas flows. The reactor's effluent was analyzed using a quadruple mass spectrometer (QMS: PrismaPlus, Pfeiffer Vacuum GmbH). For the QMS measurements, the internal pressure of the QMS was maintained constant despite changes in reactor pressure. Furthermore, we normalized the QMS signal, or ion current, using the signal of Ar gas, which served as an internal reference.

To investigate the surface reactions, the catalyst was reduced at 600 °C, purged with Ar, and then cooled to 250 °C, similar to the process described above. Then, one of the reactant gases, H_2 or CO_2, was first adsorbed on the catalyst surface. The chamber was purged again with Ar (110 mL min^{-1}) for 10 minutes for the replacement of the gas. Subsequently, another reactant gas was introduced to initiate surface reactions with and without GRD, and reaction products were detected using QMS and *in situ* TIR.

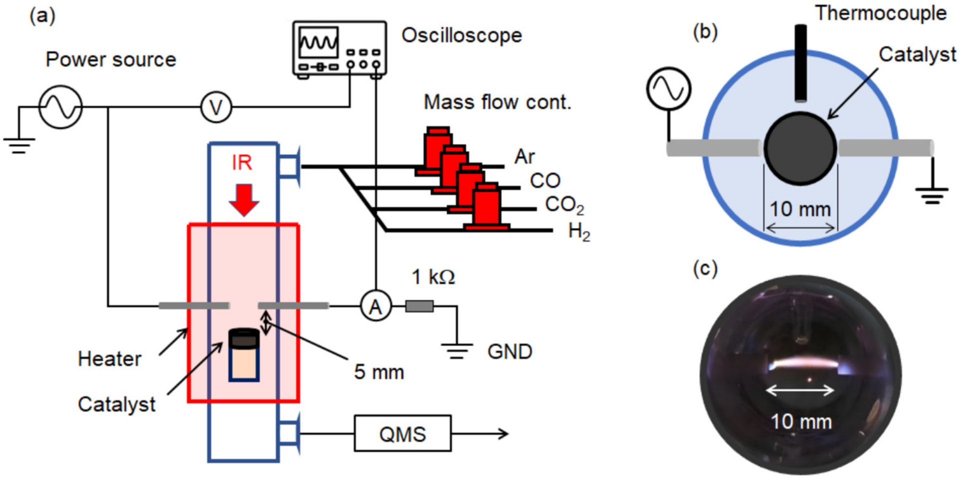

Fig. 1. Schematic diagram of (a) *in situ* TIR cell and electrode configuration; (b) cross-sectional view of the cell; and (c) GAD irradiation under $CO_2/H_2/Ar = 10/40/110$ mL min^{-1}.

3. Results and discussion

3.1 Analysis of voltage and current waveforms of GAD

The relationship between the voltage and current waveforms was analyzed to reveal the dynamic behavior of GAD. As shown in Fig. 2, the electrical signals are presented under the gas conditions of CO_2 methanation and an excitation voltage of 60 V (input voltage to the high-voltage power source). Fig. 2(a) displays the voltage and current waveforms for one cycle (50 Hz) of GAD operation (refer to the Appendix). Zoomed-in waveforms at three different phases, i.e. (b-i) breakdown phase, (b-ii) maintenance phase, and (b-iii) dissipation phase, are also displayed.

The breakdown phase is the initial phase where the voltage increases to initiate the gas breakdown. Spike-like discharge current pulses are observed at 25 kHz, the same interval of applied voltage; correspondingly, applied voltage drops abruptly. The maintenance phase follows, maintaining the constant amplitude of the applied voltage. This is a typical response of a leakage transformer that decreases the secondary voltage output as the discharge current increases. Voltage and current waveforms are synchronized, and no current peak appears, showing that gas breakdown is absent. In the meantime, positive ions generated during the breakdown phase would produce a conductive channel between electrodes. Electrical energy is consumed during the maintenance phase due to Joules loss, leading to gas heating; it is unclear whether excited species are generated during the maintenance phase. Because gas breakdown is not anticipated, emission spectroscopy or imaging techniques are not applicable to characterize the maintenance phase. Finally, the dissipation phase occurs when the conductive channel extinguishes; therefore, the discharge current is negligibly small compared to the breakdown and maintenance phases. During the dissipation phase, the applied voltage increases, initiating the breakdown phase again.

In general GAD, the electrical properties of the discharge channel vary as it elongates between the knife-shaped electrodes by the fast gas flow. Finally, the discharge channel is blown off and extinguished, producing transient arc discharge or highly non-equilibrium discharge conditions. In this study, knife-shaped electrodes were not applicable to the miniaturized IR chamber because they are too large and complex to install. Moreover, the IR setup does not accommodate a large gas flow, which is required to blow off the transient arc channel. This forces the use of small input power to generate GAD-type discharge so that a small SEI (specific energy input, kJ mol^{-1}) is maintained. To this end, the inverter-controlled leakage transformer circuit was used, which determines discharge on-and-off behavior by high-frequency (25 kHz) operation. As a result, discharge current spikes are generated as shown in Fig. 2 (b-i), pretending GAD-type discharge, although the discharge channel is generated between the point-to-point electrodes and was not blown by the fast gas flow. A high-frequency GAD is clarified into the glow mode and spark mode [23]. A glow-mode GAD is characterized by a weak discharge current of several 100 mA, while a discharge current spike reaches tens of amperes in the spark-mode GAD. In this study, because discharge current spikes are smaller than one ampere (Fig. 2 (b-i)), the discharge is characterized as glow-mode GAD, which differs from high-current spark-mode GAD generally found in the literature.

Direct measurements of plasma parameters, such as electron density and temperature, were beyond the scope of this study, which primarily focused on the effects of plasma on catalytic surface reactions in CO_2 methanation. Given that CO_2 and H_2 were the only gases supplied in our experimental setup, reactive nitrogen species (RNS) were not generated and thus not considered in this work. In the meantime, we observed evidence of reactive oxygen species (ROS), particularly atomic oxygen, when CO_2 splits into CO and O in our system. This is indicated by an increase in O_2 signal during GAD operation, as discussed in the following section, suggesting the presence and subsequent recombination of atomic oxygen into molecular oxygen. The influence of these reactive oxygen species on both gas-phase and surface chemistry is elaborated upon in the next section, providing crucial insights into the complex interactions within our plasma-catalytic system for CO_2 methanation.

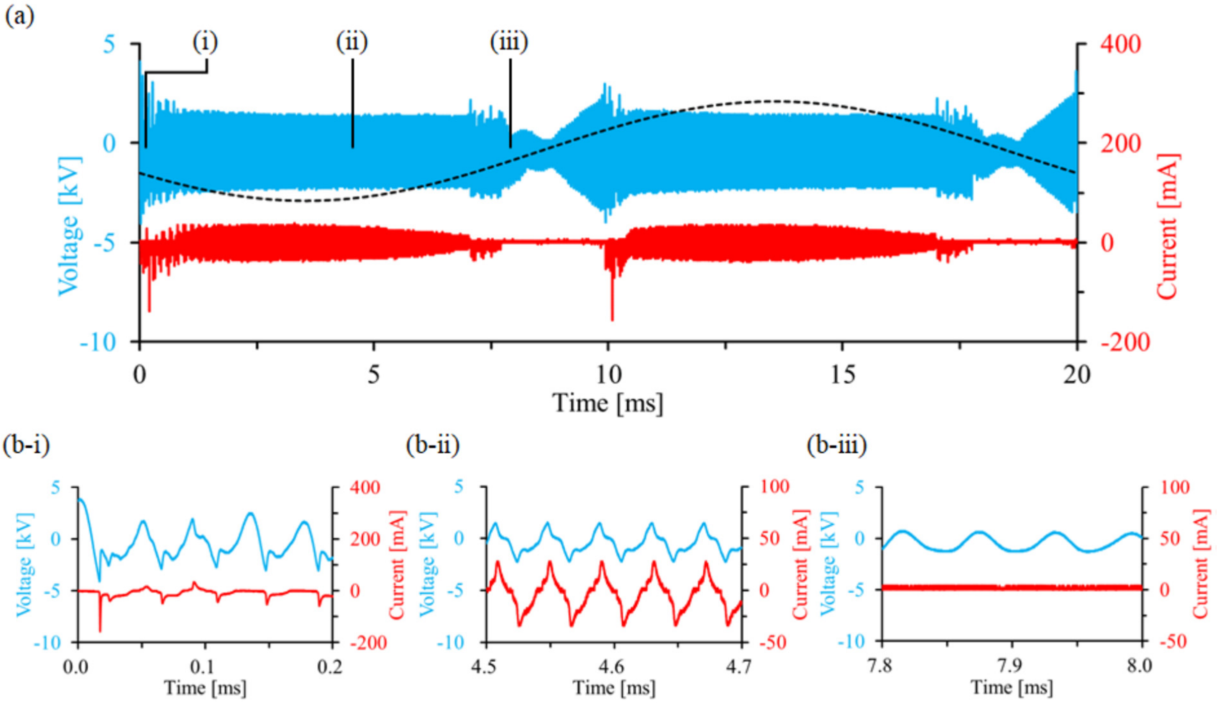

Fig. 2. (a) Voltage and current waveforms for one cycle (50 Hz) GAD operation. Zoomed-in waveforms of (b-i) breakdown phase, (b-ii) maintenance phase, and (b-iii) dissipation phase. Conditions: $CO_2/H_2/Ar = 10/40/110$ mL min^{-1}, Temperature = 250 °C.

3.2 CO_2 hydrogenation

Fig. 3 (a) and (b) respectively display the *in situ* TIR and QMS results of the hydrogenation of CO_2 under thermal and plasma conditions over Ni/Al_2O_3. For comparison, Fig. 3 (c) presents the QMS results of a blank. reference without a catalyst. In Fig. 3 (a), IR peaks appear at 2023 and 1920 cm^{-1}, which are assigned to linear and bridge bonded CO (l-CO and b-CO) at the Ni site [24–26], respectively. The additional peaks observed at 1596, 1392, and 1376 cm^{-1} are attributed to the adsorption peaks of bidentate formate (b- formate) [27, 28].

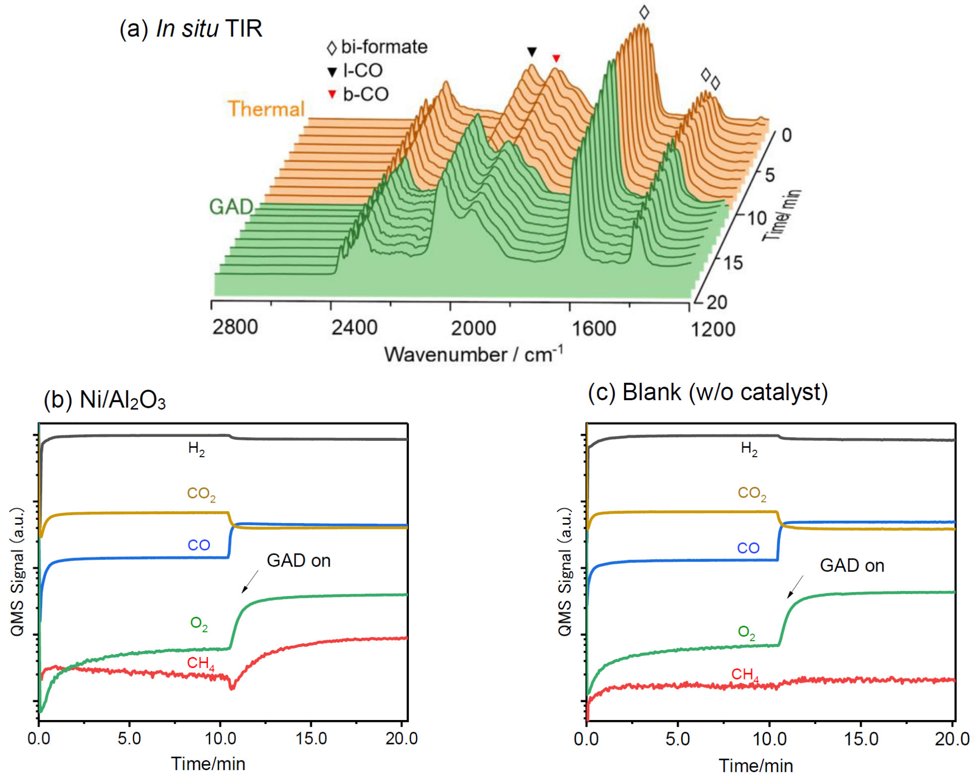

Fig. 3. Plasma enhancement of CO_2 hydrogenation identified by *in situ* TIR and QMS. (a) *In situ* TIR spectra of surface species on Ni/Al_2O_3. (b) QMS signal with Ni/Al_2O_3. (c) QMS signal with blank reference. A CO_2/H_2 mixture was introduced at a constant flow rate, while reaction conditions were switching from thermal to GAD at 10 min with 80 kPa.

Fig. 3 (a) shows that the hydrogenation reaction carried out in a thermal environment leads to the buildup of formate, and at the same time, a clear carbon monoxide peak can be observed, which is typical of the carbon monoxide gas that is complexed with Ni. Unlike noble metal catalysts, nickel surfaces are stronger for carbon monoxide adsorption, so it can produce obvious carbon monoxide peaks [29]. Upon GAD is turned on, a rapid decrease in formate adsorption is observed, along with a concomitant increase in the carbon monoxide peak, along with an increase in methane yield in the QMS results in Fig. 3 (b). It must be noted that there is a transient decrease in methane yield at the beginning of GAD application, which may be related to the lack of carbon source due to the violent gas-phase reaction (reverse water gas shift reaction or direct decomposition of CO_2) in the gas phase [30]. Combined with the results from Fig. 3 (c), these intense gas-phase reactions are solely associated with GAD, producing nearly equal amounts of CO gas under the same conditions, with CO_2 conversion of 40% for both scenarios. The overall CO_2 reduction closely matches the combined formation of CO and CH_4, within experimental error, indicating a good carbon balance in the reaction system.

Besides the production of CO, the gas-phase reactions also lead to an increase in oxygen concentration, which could further hinder the methanation of CO_2. The comparable oxygen signals in Fig. 3 (b) and (c) are attributed to the dominance of gas-phase reactions at high pressure (80 kPa). Under these conditions, GAD induces numerous gas-phase reactions, including direct CO_2 decomposition, which primarily contributes to the strong O_2 signal. The absence of a significant decrease in the oxygen signal in Fig. 3(b), despite increased methane production compared to blank conditions, can be explained by two factors. Firstly, gas-phase reactions dominate at high pressure, producing oxygen through direct CO_2 decomposition. Additionally, a portion of the decomposed CO_2 and resulting O_2 likely enters the QMS directly as outlet gas without interacting with the catalyst, resulting in a minimal difference in detected oxygen between the catalyst and blank conditions. As the formate coverage on the surface stabilizes, the methane yield also stabilizes. Unusually, although there was a significant increase in the peak of carbon monoxide initially, it then remained stable and appeared to be unrelated to the change in methane yield. This observation is correlated to the fact that carbon monoxide saturates on the catalyst surface without producing methane.

It is important to note that while the reported temperature (250 °C) represents the heater's set point, the additional heating effect of GAD on the catalyst warrants consideration. However, our thermocouple measurements did not indicate a temperature increase during GAD operation. This observation can be attributed to the feedback mechanism employed by the heater: As the temperature increases by GAD, the heater correspondingly reduces its power output, thereby maintaining a constant temperature. To ensure accuracy, we calibrated the thermocouple using a thermal camera prior to experiments. As a result, the catalyst heating effect by GAD is minimized.

To investigate the impact of different pressures on plasma catalysis, we conducted comparative experiments at 80, 40, and 10 kPa, with the results presented in Fig. 4. Fig. 4 (a) shows the *in situ* TIR spectra of plasma catalysis, while Fig. 4 (b) displays the *in situ* TIR spectra of thermal catalysis. Fig. 4 (c) and 3 (d) provide the corresponding QMS results for each. In Fig. 4 (a), the results at a reaction pressure of 80 kPa are consistent with those shown in Fig. 3 (a), where IR peaks attributed to linearly adsorbed CO (l-CO) and bridged adsorbed CO (b-CO), as well as peaks corresponding to bidentate formate, are observed. Under the reduced pressures of 40 and 10 kPa, the overall positions of the IR peaks remain largely unchanged, except for peaks near 2400 cm^{-1}, which vary due to changes in the concentration of CO_2 (from 10 kPa to 80 kPa) [27]. Comparing the QMS results in Fig. 4 (c), it is evident that the CO_2 conversion is highest at 80 kPa (approximately 42%), decreasing to 10.7% and 4.4% as the pressure decreases. The conversion of CO_2 under different pressure conditions in the catalytic reactions are detailed in Table 1.

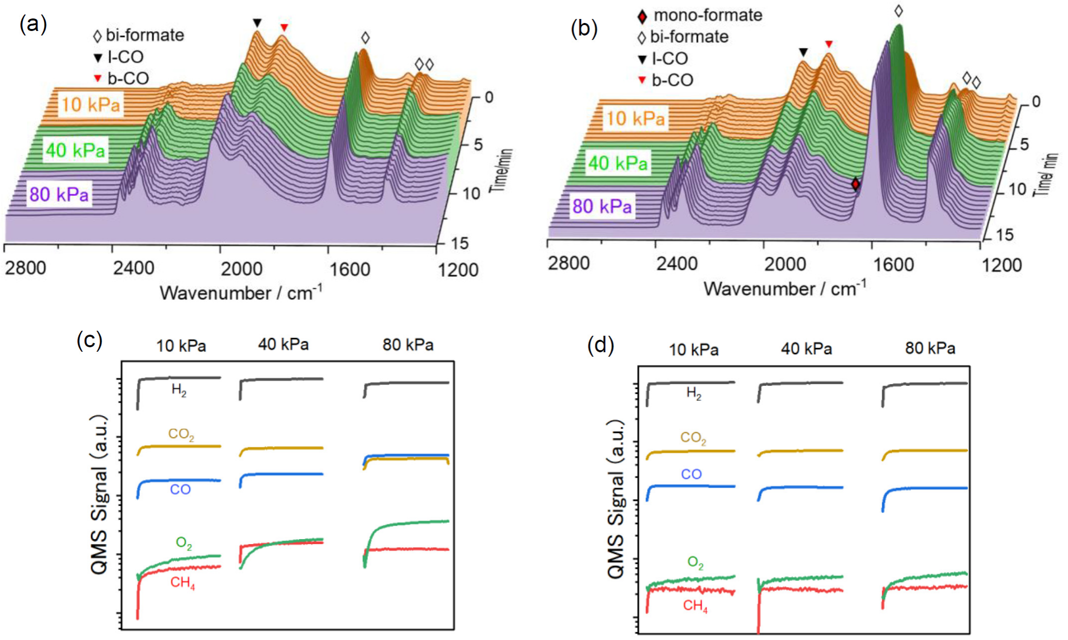

Fig. 4. Impact of different pressure conditions on plasma catalysis using a Ni/Al_2O_3 catalyst. (a) *in situ* TIR results of plasma catalysis, (b) *in situ* TIR results of thermal catalysis, (c) and (d) corresponding QMS results. The experiments were conducted at pressures of 80, 40, and 10 kPa, respectively, to explore the effect of pressure variations on the catalytic processes.

However, although the CO_2 conversion at 80 kPa is four times higher than at 40 kPa, the methane production remains consistent. Only when the pressure further decreases to 10 kPa the methane yield decrease. The consistent methane production at 80 kPa and 40 kPa, despite intensified gas-phase reactions by GAD, may be attributed to the particular reactor configuration used in this study. With only 25–30 mg of the Ni/Al_2O_3 and part of the reaction gas bypassing directly out of the reactor, surface reactions saturate [12]. Furthermore, it is important to note that although the gas flow supplied is the same under all three conditions, the actual residence time of the gas in the reactor varies due to the changes in pressure; at 10 kPa, the residence time is approximately 1/8 of that at 80 kPa. Therefore, when calculating the reaction rates based on this ratio, the methane generation rate at 80 kPa as a reference ($r_{80kPa} = 1$), the relative rate at 40 kPa is 2.74, and at 10 kPa it is 2.86. Combined with the blank reference QMS results shown in Fig. 3 (c), the relationship between pressure and methane production rate in this plasma-catalytic system exhibits a complex, non-linear behavior.

While higher pressures generally favor the methanation process thermodynamically, our results reveal an interesting phenomenon. The methane generation rate at 40 kPa surpasses that at 80 kPa, contrary to what might be expected from thermodynamic considerations. This can be attributed to the fact that higher pressures, while thermodynamically favorable, also promote complex gas-phase reactions that can potentially interfere with methane formation. As the pressure is further reduced to 10 kPa, we observe a continued increase in the methane generation rate, albeit less pronounced than the increase seen from 80 kPa to 40 kPa. This moderation in the rate increase at very low pressures likely stems from thermodynamic limitations becoming more significant. These observations underscore the delicate balance between kinetic factors influenced by plasma-induced reactions and thermodynamic constraints in determining the optimal pressure for methane production in this system.

Table 1. CO_2 conversion under different pressure in plasma and thermal catalysis.

Pressure (kPa)	CO_2 conversion (%)	
	Plasma catalysis	Thermal catalysis
80	41.2	1.9
40	10.7	2.3
10	4.4	2.1

In thermal catalysis, as observed in Fig. 4 (b), the same adsorption of CO and bidentate formate occurs, but a new IR peak appears at 1670 cm^{-1}, attributed to monodentate formate (m-formate) [31, 32]. It is observed that as the pressure increases, the accumulation of bidentate formate on the surface continues, peaking at 80 kPa, along with the accumulation of monodentate formate. Compared to Fig. 4 (a), this is the first appearance of monodentate formate, and its intensity is much higher than in plasma catalysis. According to Fig. 4 (d), under three pressure conditions at 250 °C in thermal catalysis, sufficient methane production is not achieved, with the CO_2 conversion remaining below 2.5%. Despite the presence of significant amounts of formate and carbon monoxide adsorbates on the surface, the ambient temperature is still insufficient to overcome the activation energy required for the hydrogenation reaction to proceed. This indicates that during thermal catalysis, the adsorption of carbon monoxide occurs first, due to the rapid decomposition following the combination of surface hydrogen with surface monodentate formate. When surface hydrogen is insufficient, monodentate formate transitions to bidentate formate, gradually accumulating on the catalyst surface [19]. With increasing reaction time, as surface bidentate formate saturates, the IR peak of monodentate formate becomes observable. Secondly, with the assistance of GAD, a large amount of active hydrogen is present on the catalyst surface, leading to the rapid decomposition of monodentate formate with only a small amount converting to bidentate formate. Thus, under plasma conditions, there is no continuous accumulation of bidentate formate on the catalyst surface.

Fig. 5 illustrates the variations in formate and CO adsorption peaks during argon and hydrogen gas purging, under both thermal and plasma catalysis conditions. For comparison, samples were prepared under conditions where only CO_2 was adsorbed without H_2, creating scenarios devoid of formate adsorption; the CO desorption behaviors under thermal conditions for these samples were also studied. As shown in Fig. 5 (a), the *in situ* TIR spectra indicate an accumulation of surface formate over time, consistent with previous analyses. During argon purging, the formate peaks on the surface decrease, while the CO peaks remain elevated. Comparing with Fig. 5 (c), where no formate adsorption occurs, the CO adsorption peaks rapidly diminish in the absence of formate.

Under plasma conditions, although the behavior during argon purging mirrors that of the thermal environment, during hydrogen purging, the formate adsorption observed in the thermal environment in Fig. 5a is further reduced. This is considered to be due to the further reduction of formate species under the plasma environment, which also explains the weak formate peaks during plasma catalysis. This demonstrates that plasma plays a crucial role in facilitating the transformation of adsorbed species, where the rapid conversion of formate enhances methane production. Conversely, under thermal catalysis at 250 °C, where the surface also possesses a significant amount of formate, the formate is stable and unable to undergo further transformation. This observation further supports our understanding of the reaction mechanism, demonstrating the intermediate role of formate in CO_2 methanation and highlighting the importance of surface species transformation in the overall catalytic process.

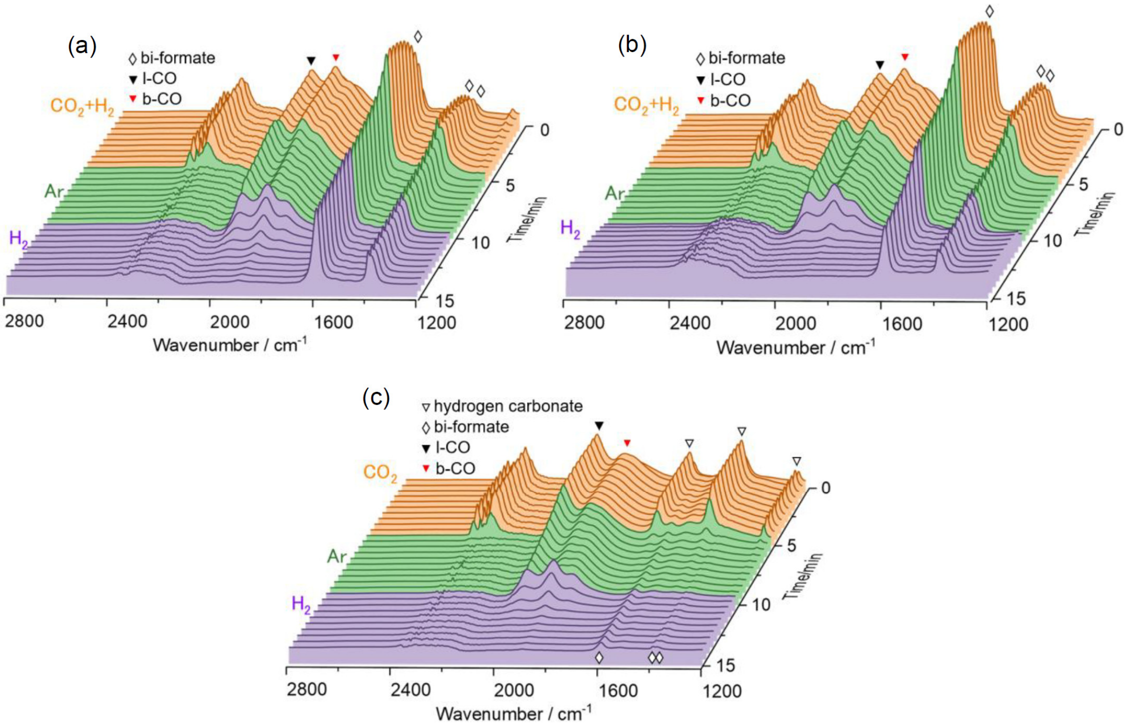

Fig. 5. Investigation of conversion characteristics of CO adsorption peaks under thermal and plasma conditions in the presence or absence of formate species on Ni/Al_2O_3 surfaces, using IR peak changes and Ar gas purging. (a) Thermal catalysis with formate, (b) Plasma catalysis with formate; for (a, b): $CO_2 + H_2 \rightarrow Ar \rightarrow H_2$, (c) Thermal catalysis without formate; $CO_2 \rightarrow Ar \rightarrow H_2$. All at 80 kPa and 250 °C.

5. Conclusion

This study has comprehensively explored the catalytic performance of Ni/Al_2O_3 under both thermal and plasma conditions, particularly focusing on the methanation of CO_2 using gliding arc discharge. The findings demonstrate significant enhancements in CO_2 conversion and methane production when utilizing Plasma, attributed to the unique interaction between the plasma environment and the catalytic surface.

Key observations from the study indicate that GAD not only improves the activation of CO_2 but also facilitates the rapid transformation of adsorbed species on the catalyst surface. This leads to an increased yield of methane compared to thermal processes, where reaction rates are generally limited by lower surface reactions speeds and kinetic constraints. The *in situ* TIR and QMS analyses have provided valuable insights. into the dynamic changes occurring during the methanation process, showing that formate species undergo rapid transformations under plasma conditions which do not accumulate as they do under thermal conditions.

Furthermore, the study has analyzed the electrical characteristics of the GAD process, capturing the dynamic voltage and current waveforms associated with the gas breakdown phenomena. The observed voltage and current profiles of GAD reveal intricate details about the arc behavior, crucial for understanding the plasma's influence on the catalytic process. Specifically, the voltage-current waveform during the breakdown phase displays spike-like discharge current pulses at 25 kHz, corresponding to abrupt voltage drops, indicating repeated gas breakdown events. During the maintenance phase, the voltage and current waveforms are synchronized without current peaks, suggesting a stable electrically conductive channel between electrodes. These electrical characteristics of GAD, combined with the catalytic data, underscore the potential of optimizing plasma catalytic systems for enhanced performance at reduced pressures. The study highlighted that while lower pressures tend to reduce the overall conversion of CO_2, they paradoxically enhance methane production due to the reduced plasma gas-phase reactions, allowing for more effective surface reactions.

In conclusion, this study not only advances our understanding of plasma-assisted catalysis for CO_2 methanation but also establishes a foundation for future research aimed at optimizing and scaling up this technology for industrial applications. The integration of Plasma catalysis could potentially revolutionize the field of sustainable chemical synthesis, offering a more efficient route for greenhouse gas utilization.

Acknowledgements

This work was supported by JST CREST (JPMJCR19R3). M. Li was supported by JST SPRING (JPMJSP2106).

References

[1] Fan W.K. and Tahir M., Recent trends in developments of active metals and heterogenous materials for catalytic CO_2 hydrogenation to renewable methane: A review, *J. Environ. Chem. Eng*., Vol. 9 (4), 105460, 2021.

[2] W. Wei and G. Jinlong, Methanation of carbon dioxide: an overview, Front. *Chem. Sci. Eng*., Vol. 5 (1), pp. 2–10, 2011.

[3] Lach D., Polanski J., and Kapkowski M., CO_2—A Crisis or Novel Functionalization Opportunity?, *Energies*, Vol. 15 (5), 1617, 2022.

[4] Feng J., Sun X., Li Z., Hao X., Fan M., Ning P., and Li K., Plasma-assisted reforming of methane, *Adv. Sci*., Vol. 9 (34), 2203221, 2022.

[5] Zhou J., Wei T., and An X., Combining non-thermal plasma technology with photocatalysis: a critical review, *Phys. Chem. Chem. Phys*., Vol. 25 (3), pp. 1538–1545, 2023.

[6] Mehta P., Barboun P., Go D.B., Hicks J.C., and Schneider W.F., Catalysis enabled by plasma activation of strong chemical bonds: a review, *ACS Energy Lett*., Vol. 4 (5), pp. 1115–1133, 2019.

[7] Nozaki T., Kim D.Y., and Chen X., Plasma-enabled electrification of chemical processes toward decarbonization of society, *Jpn. J. Appl. Phys*., Vol. 63 (3), 030101, 2024.

[8] Kim H.-H., Ayman A.A., Teramoto Y., Nozaki T., Hensel K., Mok Y.-S., Saud S., Nguyen D.B., Lee D.H., and W.S. Kang, Interim report of plasma catalysis: Footprints in the past and blueprints for the future*, Int. J. Plasma Environ. Sci. Technol*., Vol. 15 (1), e01004, 2021.

[9] Bogaerts A., Tu X., Whitehead J.C., Centi G., Lefferts L., Guaitella O., Azzolina-Jury F., Kim H.-H., Murphy A.B., Schneider W.F., Nozaki T., Hicks J.C., Rousseau A., Thevenet F., Khacef A., and Carreon M., The 2020 plasma catalysis roadmap, *J. Phys. D: Appl. Phys*., Vol. 53 (44), 443001, 2020.

[10] Ashok J., Pati S., Hongmanorom P., Tianxi Z., Junmei C., and Kawi S., A review of recent catalyst advances in CO_2 methanation processes, *Catal.Today*, Vol. 356, pp. 471–489, 2020.

[11] Jiang Y., Lang J., Wu X., and Hu Y.H., Electronic structure modulating for supported Rh catalysts toward CO_2 methanation, *Catal. Today*, Vol. 356, pp. 570–578, 2020.

[12] Ullah S., Gao Y., Dou L., Liu Y., Shao T., Yang Y., and Murphy A.B., Recent trends in plasma-assisted CO_2 methanation: a critical review of recent studies, Plasma Chem Plasma Process, Vol. 43 (6), pp. 1335–1383, 2023.

[13] Saeidi S., Najari S., Hessel V., Wilson K., Keil F.J., Concepción P., Suib S.L., and Rodrigues A.E., Recent advances in CO_2 hydrogenation to value-added products — Current challenges and future directions, Progress in *Energy Combust. Sci.*, Vol. 85, 100905, 2021.

[14] Biset-Peiró M., Mey R., Guilera J., and Andreu T., Adiabatic plasma-catalytic reactor configuration: Energy efficiency enhancement by plasma and thermal synergies on CO_2 methanation, *Chem. Eng. J*., Vol. 393, 124786, 2020.

[15] Lee C.J., Lee D.H., and Kim T., Enhancement of methanation of carbon dioxide using dielectric barrier discharge on a ruthenium catalyst at atmospheric conditions, *Catal. Today*, Vol. 293–294, pp. 97–104, 2017.

[16] Huang Q., Liang Z., Qi F., Zhang N., Yang J., Liu J., Tian C., Fu C., Tang X., Wu D., Wang J., Wang X., and Chen W., Carbon dioxide conversion synergistically activated by dielectric barrier discharge plasma and the $CsPbBr_3$@TiO_2 photocatalyst, *J. Phys. Chem. Lett*., Vol. 13 (10), pp. 2418–2427, 2022.

[17] Snoeckx R. and Bogaerts A., Plasma technology – a novel solution for CO_2 conversion?, *Chem. Soc. Rev*., Vol. 46 (19), pp. 5805–5863, 2017.

[18] Sheng Z., Kim H.-H., Yao S., and Nozaki T., Plasma-chemical promotion of catalysis for CH_4 dry reforming: unveiling plasma-enabled reaction mechanisms, *Phys. Chem. Chem. Phys.*, Vol. 22 (34), pp. 19349–19358, 2020.

[19] Kim D.-Y., Ham H., Chen X., Liu S., Xu H., Lu B., Furukawa S., Kim H.-H., Takakusagi S., Sasaki K., and Nozaki T., Cooperative catalysis of vibrationally excited CO_2 and alloy catalyst breaks the thermodynamic equilibrium limitation, *J. Am. Chem. Soc.*, Vol. 144 (31), pp. 14140–14149, 2022.

[20] Allah Z.A. and Whitehead J.C., Plasma-catalytic dry reforming of methane in an atmospheric pressure AC gliding arc discharge, *Catal. Today*, Vol. 256, pp. 76–79, 2015.

[21] Chun Y. N., Yang Y.C., and Yoshikawa K., Hydrogen generation from biogas reforming using a gliding arc plasma-catalyst reformer, *Catal. Today*, Vol. 148 (3), pp. 283–289, 2009.

[22] Zhan C., Kim D.-Y., Xu S., Kim H.-H., and Nozaki T., Nonthermal plasma catalysis of CO_2 methanation over multi-metallic Ru based catalysts, *Int. J. Plasma Environ. Sci. Technol*., Vol. 16 (3), e03006, 2022.

[23] Zhu J., Gao J., Ehn A., Aldén M., Larsson A., Kusano Y., and Li Z., Spatiotemporally resolved characteristics of a gliding arc discharge in a turbulent air flow at atmospheric pressure, *Phys. Plasmas*, Vol. 24 (1), 013514, 2017.

[24] Wadayama T., Todoroki N., Yamada Y., Sugawara T., Miyamoto K., and Iijama Y., Oxygen reduction reaction activities of Ni/Pt(111) model catalysts fabricated by molecular beam epitaxy, *Electrochemistry Communications*, Vol. 12 (8), pp. 1112–1115, 2010.

[25] Blackmond D.G. and Ko E.I., Structural sensitivity of CO adsorption and H_2/CO coadsorption on Ni/SiO_2 catalysts, *J. Catal.*, Vol. 96 (1), pp. 210–221, 1985.

[26] Primet M., Dalmon J.A., and Martin G.A., Adsorption of CO on well-defined Ni/SiO2 catalysts in the 195–373 K range studied by infrared spectroscopy and magnetic methods, *Journal of Catalysis*, Vol. 46 (1), pp. 25–36, 1977.

[27] Sibi M.G., Verma D., Setiyadi H.C., Khan M.K., Karanwal N., Kwak S.K., Chung K.Y., Park J.-H., Han D., Nam K.-W., and Kim J., Synthesis of monocarboxylic acids via direct CO_2 conversion over ni–zn intermetallic catalysts, *ACS Catal.*, Vol. 11 (13), pp. 8382–8398, 2021.

[28] Zhou R., Rui N., Fan Z., and Liu C., Effect of the structure of Ni/TiO_2 catalyst on CO_2 methanation, *Int. J. Hydrogen Energy*, Vol. 41 (47), pp. 22017–22025, 2016.

[29] Dey S., Dhal G.C., Mohan D., and Prasad R., Advances in transition metal oxide catalysts for carbon monoxide oxidation: a review, *Adv Compos Hybrid Mater*, Vol. 2 (4), pp. 626–656, 2019.

[30] Chaudhary R., Rooij G. van, Li S., Wang Q., Hensen E., and Hessel V., Low-temperature, atmospheric pressure reverse water-gas shift reaction in dielectric barrier plasma discharge, with outlook to use in relevant industrial processes, *Chem. Eng. Sci.*, Vol. 225, 115803, 2020.

[31] Yang Y., Mims C.A., Disselkamp R.S., Mei D., Kwak J.-H., Szanyi J., Peden C.H.F., and Campbell C.T., Isotope effects in methanol synthesis and the reactivity of copper formates on a Cu/SiO_2 catalyst, *Catal. Lett.*, Vol. 125 (3), pp. 201–208, 2008.

[32] Yang Y., Mims C.A., Disselkamp R.S., Kwak J.-H., Peden C.H.F., and Campbell C.T., (Non)formation of methanol by direct hydrogenation of formate on copper catalysts, *J. Phys. Chem. C*, Vol. 114 (40), pp. 17205–17211, 2010.

Supporting Information

Appendix: Characteristics of high-voltage power source

Fig. S1 shows a schematic diagram of the inverter-controlled leakage transformer circuit (Lecip Co. ALPHA NEON M-5), which generates a high voltage at about 25 kHz (Fig. 2). To characterize the performance of the high-voltage power source, the voltage output at an open circuit (without gas breakdown) was recorded as shown in Fig. S2. The envelope of the high-voltage waveform, Fig. S2(a), corresponds to the 50 Hz sinusoidal signal because the AC 50 Hz plug power was used for the primary input of the transformer (A in Fig. S1). The inverter switching circuit (B in Fig. S1) generates high-frequency alternating voltage, followed by stepping up by the leakage transformer (C in Fig. S1). A zoomed-in waveform of Fig. S2 (a) between –4.2 < t < –3.8 ms shows 18 kHz quasi-sinusoidal high voltage (Fig. S2 (b)). The frequency changes from 18 kHz to 25 kHz when the gas breakdown occurs because the discharge channel influences the impedance of the circuit.

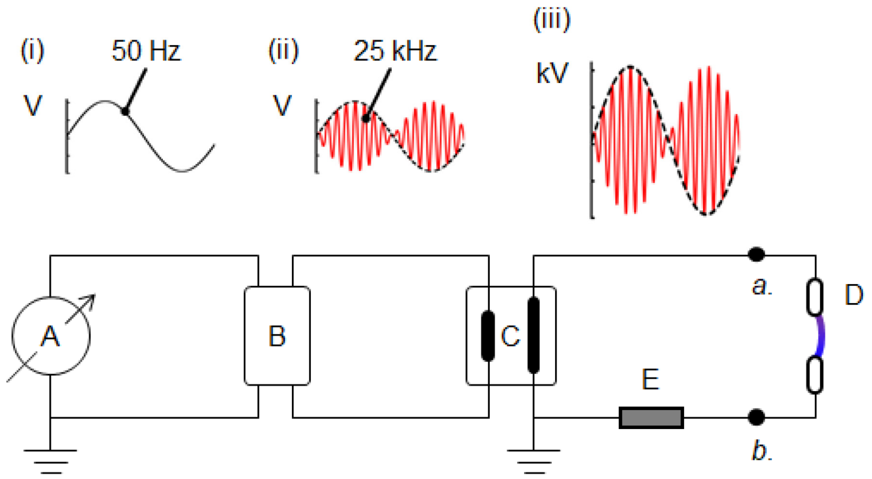

Fig. S1. Schematic diagram of the inverter-controlled leakage transformer and point-to-point electrode system. A: variable AC 50 Hz power source, B: inverter circuit, C: leakage transformer, D: point-to-point electrodes, E: electrical resistance (1 kΩ), a, b: oscilloscope measurement points.

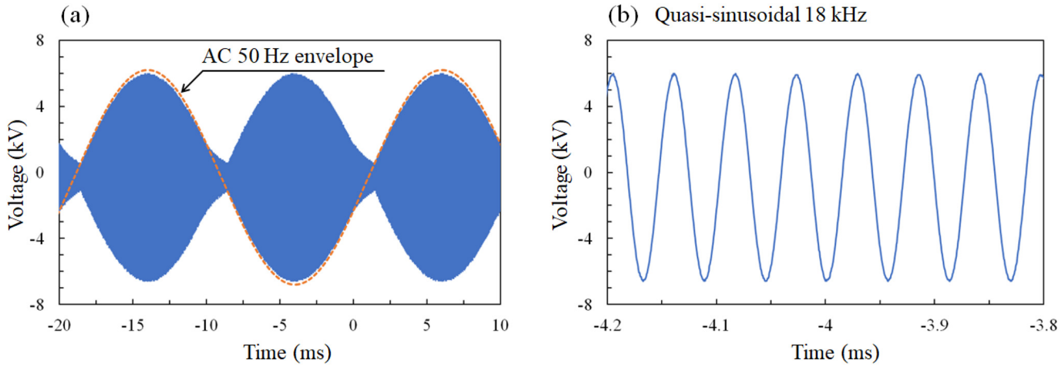

Fig. S2. (a) High-voltage waveform generated by the inverter-controlled leakage transformer (Fig. S1), (b) A zoomed-in voltage waveform between –4.2 < t < –3.8 ms.